Profiling transboundary aerosols over Taiwan and assessing their radiative effects

Sheng-Hsiang Wang,[1,2,3] Neng-Huei Lin,[1,*] Ming-Dah Chou,[1] Si-Chee Tsay,[3] Ellsworth J. Welton,[3] N. Christina Hsu,[3] David M. Giles,[4,3] Gin-Rong Liu,[1] and Brent N. Holben[3]

[1]National Central University, Chung-Li, Taiwan
[2]University of Maryland, College Park, Maryland, USA
[3]Goddard Space Flight Center, NASA, Greenbelt, Maryland, USA
[4]Sigma Space Corporation, Lanham, Maryland, USA

Submitted to the Journal of Geophysical Research – Atmospheres

Special section on East Asian Study of Tropospheric Aerosols and Impact on Regional Climate

*Corresponding author address: Dr. Neng-Huei Lin, Department of Atmospheric Sciences, National Central University, Chung-Li 320, Taiwan

Email:nhlin@cc.ncu.edu.tw

Tel and Fax : +886-3-4254069

Abstract

A synergistic process was developed to study the vertical distributions of aerosol optical properties and their effects on solar heating using data retrieved from ground-based radiation measurements and radiative transfer simulations. Continuous MPLNET and AERONET observations were made at a rural site in northern Taiwan from 2005 to 2007. The aerosol vertical extinction profiles retrieved from ground-based lidar measurements were categorized into near-surface, mixed, and two-layer transport types, representing 76% of all cases. Fine-mode (Ångström exponent, α, ~1.4) and moderate-absorbing aerosols (columnar single-scattering albedo ~0.93, asymmetry factor ~0.73 at 440 nm wavelength) dominated in this region. The column-integrated aerosol optical thickness at 500 nm (τ_{500nm}) ranges from 0.1 to 0.6 for the near-surface transport type, but can be doubled in the presence of upper-layer aerosol transport. We utilize aerosol radiative efficiency (ARE; the impact on solar radiation per unit change of τ_{500nm}) to quantify the radiative effects due to different vertical distributions of aerosols. Our results show that the ARE at the top-of-atmosphere (-23 W m^{-2}) is weakly sensitive to aerosol vertical distributions confined in the lower troposphere. On the other hand, values of the ARE at the surface are -44.3, -40.6 and -39.7 W m^{-2} for near-surface, mixed, and two-layer transport types, respectively. Further analyses show that the impact of aerosols on the vertical profile of solar heating is larger for the near-surface transport type than that of two-layer transport type. The impacts of aerosol on the surface radiation and the solar heating profiles have implications for the stability and convection in the lower troposphere.

INDEX TERMS: 0305 Atmospheric Composition and Structure: Aerosols and particles; 0360 Atmospheric Composition and Structure: Transmission and scattering of radiation; 1637

Global Change: Regional climate change; 3359 Atmospheric Processes: Radiative processes; 0345 Atmospheric Composition and Structure: Pollution: urban and regional (0305 , 0478 , 4251)

KEYWORDS: aerosol vertical distribution, aerosol optical properties, direct aerosol radiative effect

1. Introduction

Aerosols affect the Earth's energy budget by scattering and absorbing radiation (the "direct effect") and by modifying the life cycle and properties of clouds (the "indirect effect"). The complex spatial, temporal, chemical composition, physical size and shape, as well as the optical characteristics of the atmospheric aerosols cause large uncertainties in the estimation of the effects of aerosols on climate [*IPCC*, 2007; *CCSP,* 2009].

Information on the vertical distribution and the optical properties of tropospheric aerosols is required for radiative transfer calculations and is of paramount importance in understanding the effects of aerosols on climate [e.g., *Kaufman et al.,* 1997a; *Haywood and Ramaswamy*, 1998 and references therein]. To date, only a few recent studies have taken into consideration the detailed aerosol vertical distribution that was retrieved using remote-sensing techniques in estimating the radiative effects of aerosols [e.g., *Johnson et al.*, 2008; *McFarlane et al.*, 2009]. However, the often observed multi-layer aerosol transport over East Asia [e.g., *Murayama et al.*, 2004; *Chiang et al.*, 2007] can cause uncertainties in the estimation of aerosol effects on the regional climate.

Several studies have demonstrated the ability to retrieve the vertical profiles of aerosol extinction using a combination of Micro Pulse Lidar (MPL) and Sun/sky radiometer

74 measurements of aerosol optical thickness (τ) [e.g., *Welton et al.,* 2000; *Welton et al*., 2002;
75 *Campbell et al.,* 2003; *Schmid et al*., 2006; *Hayasaka et al*., 2007; *He et al.*, 2008]. The
76 NASA Micro Pulse Lidar Network (MPLNET) [*Welton et al*., 2001] provides coordinated
77 and standardized observations of aerosol vertical distribution from a federated network of
78 MPL systems collocated with the NASA Aerosol Robotic Network (AERONET) [*Holben et*
79 *al*., 1998] Sun/sky radiometers. However, at the present time only a subset of all MPLNET
80 sites have collected more than a few continuous years of data. Thus, long-term studies of
81 MPLNET derived aerosol vertical distribution are only just now becoming possible. In this
82 paper, we first demonstrate a long-term database obtained from an AERONET and MPLNET
83 collocated site to study aerosol vertical distributions of optical properties. The data
84 acquisition rate is used to evaluate the state-of-the-art measurement strategy for this site.
85
86 In this study, we present a synergistic process to characterize the vertical distributions of
87 aerosols, their optical properties, and the direct aerosol radiative effect (DARE) using
88 ground-based remote-sensing and a radiative transfer model. Three years (from 2005 to 2007)
89 of vertical aerosol extinction (σ, km^{-1}) profiles and column-integrated aerosol optical
90 properties were derived from lidar and Sun/sky radiometers measurements at a rural location
91 in Taiwan. We categorized the aerosol extinction profiles into three types, representing the
92 major characteristics of the vertical distribution of aerosol over Taiwan. The integration with
93 trajectories analysis, space-based remote-sensing and radiative transfer calculations provided
94 insights into understanding the relationships between the vertical distribution of aerosol, the
95 transport mechanism, its optical properties and its radiation effects.
96

2. Measurements and Data Usage

2.1. Site Description

The aerosol data used in this study were taken from observations at National Central University (NCU) in Chungli City (24.97°N, 121.18°E; 133 m above sea level), 50 km south of Taipei, Taiwan. Chungli is a medium-sized city with a population of ~360,000. NCU serves as a rural site because it is located at the western edge of Chungli with no significant emission sources nearby. The meteorological conditions are characterized by the southwesterly Asian monsoon in the summer and the northeasterly monsoon in the winter. The weather is humid and cloudy during the summer, but dry and relatively clear during the winter. Studies have shown that northern Taiwan is located on the pathway of the pollution transport from Asia to the Pacific Ocean during pollution outbreaks [*Liu et al*., 2006; *Chiang et al.*, 2007].

2.2. Sun/sky radiometer

The CIMEL Electronique CE-318 Sun/sky radiometer measurements reported in this paper were made by instruments that participate in AERONET [*Holben et al*., 1998]. A brief description of the instrumentation and its calibration can be found on the AERONET website (http://aeronet.gsfc.nasa.gov/). The Sun/sky radiometer makes direct solar irradiance measurements with a 1.2° full field of view every 15 min at 340, 380, 440, 500, 675, 870, 940, and 1020 nm (nominal wavelength, λ). The uncertainty of the measured τ, due primarily to the calibration uncertainty, is ±0.01 for λ>440nm and ±0.02 for $\lambda \leq$440nm. In addition to the direct solar irradiance measurements, the Sun\sky radiometer measures the sky radiance at four wavelengths (440, 675, 870, and 1020 nm) along the solar almucantar (i.e., at a constant

120 elevation angle, with varied azimuth angles) up to eight times a day. The sky radiance
121 measurements are used to retrieve additional columnar aerosol properties including volume
122 size distribution, phase function, real and imaginary components of the refractive index,
123 effective particle radius, single-scattering albedo (ω), and the asymmetry factor (g), which are
124 routinely computed with the AERONET inversion algorithms [*Dubovik and King*, 2000;
125 *Dubovik et al.*, 2006; *Holben et al.*, 2006]. Specifically, the retrievals of ω and the imaginary
126 part of the refractive index are further limited to $\tau_{440nm} \geq 0.4$ due to an increased uncertainty
127 in the absorption properties of the inversion retrieval during a lower aerosol loading in the
128 atmosphere [*Dubovik et al.* 2002a and 2002b]. The uncertainty in the retrieved ω is estimated
129 to be ±0.03.
130
131 Two Sun/sky radiometers are located at the NCU campus. One of them is jointly
132 operated by the Taiwan Environmental Protection Administration (EPA) and the Department
133 of Atmospheric Sciences, NCU (hereafter referred to as the EPA-NCU site). The other
134 radiometer, located within ~200 m of the EPA-NCU site, is operated by the Center for Space
135 and Remote Sensing Research, NCU (hereafter referred to as the NCU_Taiwan site).
136
137 **2.3. Micro Pulse Lidar (MPL)**
138 The EPA-NCU MPL system is a member of the NASA MPLNET project
139 (http://mplnet.gsfc.nasa.gov/). The MPL [*Spinhirne et al*., 1995] is a compact and eye-safe
140 single wavelength (527 nm) elastic backscatter lidar system capable of determining the range
141 of both aerosols and clouds by firing a short pulse of laser light and measuring the
142 time-of-flight from the pulse transmission to the reception of the returned signal. Our system

supports long-term measurements with 1-minute time resolution and 0.075 km vertical resolution. The standard instrument design and level 1 signal processing are described in detail by *Campbell et al*. [2002] and *Welton et al.* [2002]. Real time data products (level 1.5, no quality assurance) are provided on a next day basis, and include identification of multiple cloud layer heights (base and top), the planetary boundary layer (PBL) height, and the height of the highest aerosol layer. Time resolutions for each product are: clouds (1 minute), aerosols (20 minutes), and PBL (5 minutes). The derivation of level 1.5 aerosol properties is based on the algorithm by *Welton et al*. [2000] where the AERONET level 1.5 aerosol optical thickness is used as the constraint to solve for the lidar ratio and the extinction and optical thickness profiles from the cloud screened 20-minute signal averages. The mean uncertainty in MPLNET retrieved extinction is ± 0.015 km^{-1}. However, the assumption of a constant lidar ratio (extinction-backscatter ratio) throughout a profile causes a larger uncertainty in the derivation of extinction when there is multi-layer aerosol transport [*Welton et al.*, 2002].

Level 2 quality-assured data products are currently under development, and beta level 2a aerosol data were made available for this study. Level 2a processing uses AERONET level 2 [*Smirnov et al.,* 2000; *Dubovik et al.*, 2002a; *Holben et al.*, 2006] aerosol optical thickness, and bad data are discarded in order to assure high quality. MPLNET data are discarded if one or several of the following occurs: the data were acquired outside the preferred instrument temperature range (22.5 ± 2 °C, for this instrument); the lidar ratio error was larger than 30%; less than 80% of the signals in the 20-minute average were cloud free; or the signal-to-noise ratio was higher than 20% directly above the top of the aerosol layer. MPLNET aerosol products have been validated in a number of studies, and the most recent and comprehensive

166 one was by *Schmid et al.* [2006], which indicated the accuracy of beta level 2a MPLNET
167 aerosol extinction profiles to within 20%.
168
169 **2.4. Data Usage**
170 The three years (from 2005 to 2007) of aerosol data (τ, α, ω, g, and σ) used in this
171 study were based on the AERONET level 2 and MPLNET beta level 2a data sets, which were
172 quality-assured and were only for cloud-free conditions. Figure 1a shows the number of days
173 in a month when the AERONET level 1 (not cloud-screened or quality-assured) and level 2
174 data were available at the two sites (EPA-NCU and NCU_Taiwan). The AERONET data from
175 EPA-NCU were not available prior to 18 July 2006. Therefore, the data from the
176 NCU_Taiwan site were used for this period. Three major issues affected the continuity of this
177 data set: (1) relatively few data were obtained from NCU_Taiwan because this site did not
178 follow closely the AERONET standard measurement procedure for continuous monitoring
179 prior to 2009, (2) the Level 2 data from NCU_Taiwan were eliminated due to an instrumental
180 issue (i.e., moisture contamination) during January and June 2006, and (3) a regular
181 calibration was performed for the EPA-NCU instrument during September and October 2007,
182 and there were no observations during these two months.
183 In Figure 1b, the MPLNET level 1 data set reveals the continuous measurements (day
184 and night) with a total of 1034 days over 3 years (a data acquisition rate of 94 %). On the
185 other hand, the MPLNET beta level 2a shows only 189 days over 3 years (a data acquisition
186 rate of ~17%), because the MPLNET beta level 2a retrieval relies on AERONET level 2 data,
187 which is cloud-screened and quality-assured data. In addition, if we consider a perfect
188 measurement period (August 2006 to July 2007) when the MPL and the Sun/sky radiometer

189 operated continuously, then the AERONET level 2 and MPLNET level 2a data for the
190 EPA-NCU site are 175 (~48%) and 119 (~33%) days per year, respectively. The value of 33%
191 represents the percentage of days with clear sky in a year and also the maximum available
192 days based on the measurement strategy for this site.
193
194 Daily mean profiles were computed when at least three σ profiles were available in a
195 UTC day. There were a total of 145 daily mean σ profiles available at NCU for the analysis
196 of the vertical characteristics of the aerosol. The daily mean values of τ, α , ω, and g for the
197 145 days were calculated from

198 $$\bar{x}_{\lambda} = \frac{1}{n} \cdot \sum_{i=1}^{n} x_{\lambda,i} \quad (1)$$

199 where $x_{\lambda,i}$ is the i^{th} instantaneous observation for aerosol optical property x at the wavelength
200 λ, and n is the number of observations in a day. Due to a large variation in the days available
201 in each month, it is not proper to interpret the seasonal variation of the vertical distributions
202 of aerosol; and therefore, a classification for the vertical distribution of aerosol has been
203 applied in this study.
204
205 **3. Methodology**
206 **3.1. Vertical Distribution Classifications of Aerosols**
207 The σ profiles derived from the MPL observations were classified into three types in
208 order to describe the complex characteristics of aerosol vertical distributions. The rules for
209 the classification of these three types are listed in Table 1. Figure 2 shows the σ profiles of
210 the three types and the corresponding temperature and dew-point profiles. In Figures 2a–2c,

211 the daily mean σ profiles conform to the rules shown in Table 1, but the instantaneous σ
212 profiles show perturbations. The corresponding temperature and dew point temperature
213 profiles shown in Figures 2d–2f are the soundings at the Taipei station (~30 km north of
214 NCU). In Figures 2a and 2d (Type 1), the vertical distribution of mean σ is restricted to
215 within 2.0 km above ground level (AGL), which is known as the mixed layer [*Stull*, 1998].
216 The sounding profiles show a strong and stable inversion layer around 2.0 km, which
217 confines aerosols to the region below 2.0 km. On the other hand, in Figure 2e, the sounding
218 profiles show an inversion layer around 1.7 km, which confines most of the aerosols in the
219 mixing layer (Figure 2b). In addition, a weaker mean σ was observed in the lower free
220 atmosphere (the layer of 1.7 - 2.8 km height in Figure 2e). This suggests that the source of
221 aerosol in the lower free atmosphere could be caused by three mechanisms: (1) the local
222 aerosols lift up to the free atmosphere from the mixing layer, (2) the aerosols remain in the
223 residual layer and (3) the long-range transport of the aerosols in the free atmosphere.
224
225 Normally, mechanisms (1) and (2) can be identified based on the time evolution of
226 normalized relative backscatter (NRB) obtained from the MPLNET level 1 data. However, to
227 define the third mechanism, we need assistance from other information (such as back
228 trajectory, sounding and satellite data). For the Type 2 case (Figures 2b and 2e), the weaker
229 inversion layer of around 1.7 km and the well following ambient temperature and dew-point
230 profiles below 2.8 km imply the exchange of air mass between the mixing layer and the lower
231 free atmosphere, as evidenced by the NRB. However, in this case the contribution from the
232 long-range transport of aerosol in the free atmosphere is hard to separate. Compared to the
233 Figure 2b, Figure 2c (Type 3) shows enhanced σ between 2 and 4 km, which is most likely

due to the long-range transport aerosol in the lower atmosphere. The strong inversion layer around 1.8 km, and the diverging ambient temperature and dew-point profiles between 2 and 3 km in Figure 2f provide evidence of the different sources of air mass in the vertical distribution. According to the characteristics of the vertical distributions of aerosol, in this paper Type 1 will refer to near-surface aerosol transport, Type 2 will refer to near-surface aerosol transport with upper-layer convective mixing/dispersion of aerosol, and Type 3 will refer to two-layer aerosol transport.

3.2. Radiative Transfer Model Calculations

We investigated the aerosol radiative effect using the radiative transfer model of *Chou and Lee* [1996] and *Chou and Suarez* [1999]. The model includes the absorption by ozone, water vapor, oxygen and CO_2, as well as the absorption and scattering by clouds, aerosols, and molecules (Rayleigh scattering). Fluxes are integrated virtually over solar spectrum, ranging from 0.175 μm to 10 μm, which is divided into 11 bands in the model. Depending upon the nature of the absorption, different approaches are applied to different absorbers. A more detailed description of this model can be found elsewhere [*cf. Chou and Suarez,* 1999; *Chou et al.,* 2006].

Data input to this model includes the vertical profiles of temperature, humidity, ozone, surface albedo and the aerosol optical properties. In this study, we constructed 121 pressure layers in vertical, starting from the ground surface and ending up at the top-of-atmosphere (TOA), in which the layers of 1-81 (from surface to ~6 km AGL with the vertical resolution of 0.075 km) were based on the vertical profile of the MPL measurement. The temperature

and humidity profiles taken from the 6-hourly NCEP reanalysis [*Kalnay et al*., 1996] were interpolated to the model layers. The vertical ozone distribution was based on the climatology values. The daily surface albedo data [*Schaaf et al.*, 2002] were derived from the moderate resolution imaging spectroradiometer (MODIS) Collection 5 combined Level 3 16-day Albedo Products (MCD43B, http://ladsweb.nascom.nasa.gov/).

The seven Cimel channels are located within the 11 bands of the radiative transfer model of *Chou et al.* [2006]. We derived the aerosol optical properties of a model band by averaging the AERONET-retrieved aerosol optical properties (i.e., τ, ω and g) within the band. For those model bands outside the range of the Cimel channels, the aerosol optical properties were set to be equal to those of the nearest Cimel channels [*Chou et al.*, 2006]. Thus, the vertical profiles of τ were derived by scaling the daily mean τ at each Cimel channel with the MPLNET-retrieved σ vertical profiles at 527 nm. For the ω and g, we assumed constant values in the vertical distribution. Because of the presence of clouds, aerosol retrievals may not be complete in a day. It is therefore not feasible to derive the aerosol radiative effect using diurnal variations of the aerosol optical properties. Instead, we used the daily mean values of aerosol optical properties to derive hourly solar radiation, and then averaged to obtain the corresponding daily mean solar radiation.

The direct aerosol radiative effect (DARE, W m^{-2}) is defined as the change in net radiation due to aerosols in clear-sky given by

$$DARE(p) = F_{wa}(p) - F_{na}(p) \quad (2)$$

where $F_{wa}\ (p)$ and $F_{na}\ (p)$ represent the net downward fluxes with and without aerosols at pressure level p. Let $DARE_{TOA}$ and $DARE_{SFC}$ be the DARE at the TOA and the surface, respectively, the DARE in the atmosphere, $DARE_{ATM}$, which is the solar heating of the atmosphere due to aerosols, is then given by

$$DARE_{ATM} = DARE_{TOA} - DARE_{SFC} \quad (3)$$

Finally, the impact of aerosols on the atmospheric heating rate of a layer between p and $p+\Delta p$, $\Delta Q\ (p)$, is proportional to $DARE(p) - DARE(p+\Delta p)$.

4. Results and Discussion

4.1. Vertical Distribution of Aerosols

Three types of σ profiles were classified based on the conditions described in section 3.1. These 3 types were found in 28, 51, and 31 days, respectively, and comprised 76% of the 145 days. The vertical profiles of the mean and standard deviation of the σ of Types 1–3 are shown in Figures 3a–3c, respectively. Below 337.5 m AGL, no readings of the σ are shown due to the near-field observation limits of our particular MPL [*Campbell et al.*, 2002]. Specifically, the average calculation for the daily σ profiles not only smoothes the profiles, but also eliminates some peak values. In addition, the large standard deviation shows that the classification we applied in this study is an approximation. The following sections provide a brief discussion of the σ profiles type classifications in relation to the backward trajectories for each type.

303

304 *Type1: Near-surface aerosol transport*

305 In Figure 3a, the mean σ decreases with the increase in height, and is restricted within
306 2.0 km. The highest σ shows ~0.2 km^{-1} near 0.5 km and decreases to ~0.01 km^{-1} at ~2.0 km.
307 The height of 2 km represents the maximum mixing layer height for Type 1, in which the
308 mixing layer height varies between 1.0 km and 2.0 km as illustrated by the standard
309 deviations of profile. In addition, the fall and winter seasons (September - January) are
310 prevailing seasons for the Type 1 classifications (Figure 3d), but few days were observed in
311 the summer time.

312

313 Trajectory analysis has been used to diagnose the movement of pollutants in previous
314 studies [e.g., *Draxler,* 1996; *Wang et al.,* 2007 and references therein]. The Hybrid
315 Single-Particle Lagrangian Integrated Trajectory (HYSPLIT) model, developed by NOAA
316 Air Resources Laboratory [*Draxler and Rolph*, 2003], is applied to calculate air mass back
317 trajectories. The meteorological data used to initialize HYSPLIT is obtained from the NCEP
318 Global Data Assimilation System (GDAS) data set [*Kalnay et al*., 1996]. Figure 4 shows the
319 5-day backward trajectories of Types 1–3 ending at 0.5 km and 2.5 km above the mean sea
320 level (MSL) over NCU. The altitudes of 0.5 km and 2.5 km present the near-surface and
321 upper-layer air mass transport, respectively. The color table uses in the image denotes
322 trajectory altitudes for the 5-day computational period. The symbols mark the days behind the
323 ending day.

324

325 In Type 1 (Figure 4a), the major pathway of the air mass shows the potential aerosol

source regions from northeast Asia with trajectories passing over the West Pacific. The four trajectories that strayed from the major pathway correspond to the days in spring and summer as shown in Figure 3d. Most of the trajectories traversed over coastal regions which have been identified as major anthropogenic regions in East Asia [*Street et al.,* 2003]. When the air mass traversed over the ocean during the last two days, the trajectories were found to be mainly within the marine boundary layer (below 1.0 km in the color table). The near surface shallow transport with anthropogenic aerosol (e.g., sulfate and nitrate) over the ocean is expected to have more aerosol water uptake or more aerosol hydroscopic growth [*Seinfeld,* 1986]. In the final half day before ending at NCU, the trajectories pass over northern Taiwan where the local pollutants also contribute to the aerosol loading. In general, the Type 1 classifications are represented by the northerly flow causing a transport belt for air mass advection over long distances towards Taiwan. The σ below 2 km are due to the presence of an abundance of anthropogenic aerosols caused by long-range transport and local pollutants.

Type 2: Near-surface aerosol transport with upper-layer convective mixing/dispersion of aerosols

In Figure 3b, the mean σ decreases with the increase in height, and is restricted to within 4.0 km. The two σ peaks below 1.0 km with a value of ~0.27 km^{-1} illustrated the various maximum σ heights in Type 2 cases. Compared to Type 1, the mean σ profile of Type 2 shows an aerosol layer that is extended up to 4 km. The upper-layer aerosol transport related to the convective mixing/dispersion of aerosols in the free atmosphere is described in Section 3.1. Figure 3e shows the diverse coverage for months in Type 2, in which the most frequent occurred month is July.

The 5-day backward trajectories at 0.5 km of NCU for Type 2 are shown in Figure 4b. Most of the trajectories come from the north of Taiwan via a route similar as that of Type 1. This implies that similar atmospheric features may represent the near-surface aerosol transport observed in both Types 1 and 2. In addition, some of the southern and eastern trajectories related to the summer season also belong to Type 2. These trajectories originate from the clean marine atmosphere and from the atmosphere in Southeast Asia where low pollution emissions are found during the summer. As a result, local emissions might be the essential source of the near-surface aerosol layer. For the upper-layer transport, as shown in Figure 4d, the trajectories ending at 2.5 km show various routes and are mostly westerly in winter and southeasterly in summer. These westerly trajectories will have traveled over densely populated and industrialized areas. In these regions the air motion transports the aerosols to the free atmosphere by means of frontal lifting [e.g., *Bey et al.*, 2001; *Liang et al.*, 2004]. On the other hand, the southeasterly trajectories which originated above the West Pacific Ocean, pass over the Philippines, the South China Sea, off the coast of southern China, and then over southern Taiwan. Most likely the marine pathway has less long-range transport aerosols from the continental regions, but a higher possibility of local aerosol aloft due to the enhanced vertical convection mixing of aerosols in summer. However, the aerosol particles that lift towards the free atmosphere are not able to be seen in the HYSPLIT simulation because of the coarse resolution of the meteorological data, as well as the terrain data.

Type 3: Two-layer aerosol transport

The two-layer transport structure of aerosols has been reported in the literature [e.g.,

372 *Welton et al.*, 2002; *Murayama et al.*, 2004; *He et al.,* 2008; *Johnson et al.,* 2008; *McFarlane*
373 *et al.,* 2009]. An MPL retrieved mean σ profile with a 2-layer structure (Type 3) over NCU is
374 shown in Figure 3c. In contrast to Type 2, Type 3 shows significant upper-layer (2–4 km)
375 aerosol transport. The prominent σ of ~0.09 km^{-1} at 2.4 km reveals almost one-half the
376 amount of ~0.21 km^{-1} near the ground, thereby emphasizing the importance of upper-layer
377 transport. We suggest that the 2-layer aerosol transport is not only due to considerable
378 quantities of long-range transport aerosols exist in the free atmosphere but also the fact that
379 inversion layer plays a significant role in preventing the mixing of vertical convective aerosol.
380 Figure 3f shows that except for the unusual occurrence of a frequency of 10 days in October
381 which related to a single event during 11 - 23 October 2006, the most frequent occurrence for
382 2-layer aerosol transport season take place in spring (March – May), which agrees with
383 previous studies in this region [*Murayama et al.*, 2004; *Chiang et al.*, 2007].
384
385 The trajectory distribution of Figure 4c shows a distribution similar to that of Figure 4b,
386 which implies that the near-surface aerosol transport has similar aerosol characteristics for
387 Type 2 and Type 3. In terms of backward trajectories at 2.5 km in Type 3 (Figure 4e), the
388 westerly trajectories suggest that westerlies prevail in the middle troposphere over
389 mid-latitude East Asia. Most of the trajectories originate in Indochina and travel slowly over
390 Southeast China during the last three days. In their pathway, air masses are likely to carry
391 biomass-burning aerosols from Indochina and mix them with the abundance of anthropogenic
392 aerosols from Southeast China and then advect them downwind towards northern Taiwan in
393 the lower free atmosphere. The spatial distribution of τ from the MODIS measurement will
394 be further applied to understand the sources region of aerosol in the next subsection.

395

396 **4.2. Spatial Distribution of Aerosol Optical Thickness**

397 The MODIS-Aqua Level 3 data with 1°×1° resolution were obtained from the Giovanni
398 online data system (http://disc.sci.gsfc.nasa.gov/giovanni/) in order to analyze the spatial
399 distribution of aerosols in relation to each classified type. MODIS sensors perform near
400 global daily observations of aerosols and eight of the 36 channels (between 0.412 and 2.13
401 μm) are used to retrieve aerosol properties over land [*Kaufman et al.*, 1997b; *Hsu et al.*, 2004
402 and 2006; *Levy et al.*, 2007] and ocean [*Tanré et al.*, 1997]. Figure 5 shows that the
403 MODIS-Aqua Level 3 aerosol retrievals of averaged τ at 550 nm for Types 1–3 in the Asian
404 region. Based on the trajectory analysis in previous section, a lead-time of three days was
405 selected for MODIS-retrieved τ to compute the average for each Type of aerosol transport.
406

407 The main locations of the large τ in Figures 5a–5c (coastal regions of China, central
408 China, and the Indo-Gangetic Plain) correspond with the relatively densely populated and
409 industrial areas. The potential aerosol sources at NCU for each type can be further illustrated
410 by combining them with the back trajectory in Figure 4. In Figure 5a, the high τ (~1) over the
411 northeastern coast of China (near 35°N, 118°E) have a high probability of contributing to the
412 near-surface aerosol transport in Type 1. On the other hand, it is evident from the Figures 5b
413 and 5c that τ are higher than those over the Asian continent and with a stronger continental
414 outflow over the Yellow Sea (near 36°N, 123°E). According to the suggestion of trajectory
415 analysis, the air masses of the near-surface aerosol transport of Type 2 traversing over the
416 high τ region in northeastern China appear more frequently indicating a higher mean σ of
417 near-surface aerosol transport in Type 2 (Figure 3b). On the other hand, the high τ over

418 southeastern China conform to the potential pollution source regions of the upper-layer
419 aerosol transport in Type 3. The high τ over southeastern China are related to the local
420 emission sources [*Street et al*., 2003] and the transported smoke aerosols from the biomass
421 burning in Southeast Asia in the spring [*Hsu et al.*, 2003; *Wang et al.,* 2007].
422
423 **4.3. Aerosol Optical Thickness and Ångström Exponent**
424 Table 2 shows the average and standard deviations of aerosol optical properties for
425 Types 1–3. The mean values of τ_{500nm} are 0.28, 0.45, and 0.44 for Types 1–3, respectively,
426 and are related to the integrated σ profiles. On the other hand, the $\alpha_{440\text{-}870nm}$ remains nearly
427 constant with a mean of ~1.4 for these 3 types, implying that fine mode particles dominate
428 the pollutants. Fine mode particles are commonly observed in the long-range transport of
429 anthropogenic aerosols [*Eck et al.*, 2005].
430
431 Figure 6 presents the scatter plots of the AERONET-retrieved daily mean $\alpha_{440\text{-}870nm}$ vs.
432 τ_{500nm} for Types 1–3. The error bars present a one standard deviation. Basically, most data
433 have $\alpha_{440\text{-}870nm}$ values within the range of 1.0–1.8, except for 2 days with lower $\alpha_{440\text{-}870nm}$ (<
434 1.0) of Type 2, implying that the common feature of fine mode aerosols dominate the
435 pollutants for those 3 classified types. However, the two days with low $\alpha_{440\text{-}870nm}$ reflect the
436 occurrence of coarse mode particles in Type 2. In the case of lowest $\alpha_{440\text{-}870nm}$ (~0.8) on 5
437 July 2007 in Figure 6b, the aerosols may possibly have been contaminated by cirrus clouds
438 [*Smirnov et al*., 2000]. The other low $\alpha_{440\text{-}870nm}$ case in Figure 6b happened on 28 January
439 2007, when an Asian dust storm was reported by Taiwan EPA. In terms of aerosol loading,
440 the ranges of τ_{500nm} show 0.13–0.63, 0.15–1.05, and 0.13–1.17 for Types 1–3, respectively.

Similar minimum values of τ_{500nm} suggest that those 3 classified aerosol profiles can be observed even in a low aerosol loading atmosphere. On the other hand, the cases with τ_{500nm} higher than 0.6 are only found in Types 2 and 3. Those high τ_{500nm} cases are not only caused by the upper-layer aerosol transport but also by the stronger aerosol emission sources shown in Figure 5. Consequently, we suggest that a fairly near-surface aerosol transport can contribute to the daily mean τ_{500nm} reaching as high as 0.6. However, when a daily mean τ_{500nm} greater than 0.6 is observed, it implies that an upper-layer aerosol transport could occur, and that the aerosol vertical distribution should be further considered for estimating the radiative effect of aerosol.

4.4. Single-scattering Albedo and Asymmetry Factor

The estimated DARE of the Earth-atmosphere system has to rely on data sources for ω and g, and especially the data on ω are particularly critical for determining the partition of the DARE between the atmosphere and the underlying surface [*Chou et al*., 2006]. By definition, ω is obtained by dividing the aerosol scattering coefficient by the aerosol extinction coefficient, and g is the fraction of the incident radiation scattered forward after striking an aerosol. g = 1 if 100% of the incident radiation is scattered forward, whereas the g = 0 indicates that one half of the incident radiation is forward-scattered while the other half is backscattered. The spectral ω and g for Types 1–3 are plotted in Figure 7. Valid data have been selected by the AERONET level 2 inversion data described in section 2.2, and the numbers of the daily mean for Types 1–3 are 4, 24, and 10 days for ω, and 20, 38, and 19 days for g. Group-mean spectral ω and g are derived by averaging arithmetically all the available daily-mean values of ω and g of a given type. The group-mean and one standard

464 deviation of ω and g at 440 nm for Types 1–3 are listed in Table 2.

465

466 In Figures 7a–7c, most of the daily mean ω ranging from 0.90 to 0.98 in any wavelength
467 shows that the aerosols are moderately absorbing. In comparison, *Eck et al.* [2005] indicated
468 that in Beijing (China) and Anmyon Island (Korea) the ranges of ω were within 0.84–0.92
469 and 0.88–0.95, respectively, suggesting that the aerosols had a stronger scattering property at
470 NCU. The stronger scattering property (higher ω) could be caused by hygroscopic growth but
471 also with other possible aging mechanisms such as gas-to-particle conversion, condensation,
472 and coagulation [*Eck et al.,* 2005].

473

474 The characteristic of the ω changing with the increase in wavelength relates to the
475 aerosol types for each individual day as shown in Figures 7a–7c. The relationships between
476 spectral dependence of ω and the key aerosol types (e.g., urban-industrial, biomass-burning,
477 desert dust and marine aerosols) have been described in *Dubovik et al.* [2002a], and are based
478 on eight years of worldwide distributed data from the AERONET network. In Type 1, the
479 characteristics of spectral dependence of ω exhibit two different types of aerosol (Figure 7a).
480 Two days (30 – 31 January 2007) with the ω increasing with the increase in wavelength
481 represented the characteristic of desert dust aerosols [*Dubovik et al.,* 2002a; *Eck et al.,* 2005],
482 and has also been identified as a dust event by the Taiwan EPA announcement. On the other
483 hand, the other two days with the ω decreasing with the increase in wavelength show that the
484 characteristic of the urban-industrial aerosol [*Dubovik et al.,* 2002a], and the values of ω
485 show comparable ranges to those of Anmyon Island in Korea [*Eck et al.,* 2005]. For Type 2,
486 most days presented the urban-industrial aerosol type, but a few days presented the desert

487 dust aerosol type. A case with an extreme low ω, with the characteristic of the ω decreasing
488 with the increase in wavelength was observed on 29 March 2007, which was linked to the
489 biomass-burning aerosols type described in *Dubovik et al.* [2002a]. Compared to Types 1 and
490 2, Type 3 (Figure 7c) shows lower spectral dependence of ω with higher ω values ranging
491 from ~0.92 to 0.97. This implies that the aerosols in the upper-layer likely have a stronger
492 scattering property. Overall, the spectral dependence of ω shows that the downwind area of
493 Asian continental pollutants is dominated by urban-industrial aerosols of three types.
494 However, the observed desert dust, the biomass-burning and the mixing aerosols emphasize
495 the complex aerosol types in this region.
496
497 In Figures 7d–7f, most of the daily mean g ranged from 0.60 to 0.75 in any wavelength
498 inhibit the aerosols tend to scatter more energy forward. The spectral dependence of g
499 decreases with the increase in wavelength, illustrating that the aerosols have more forward
500 scattering in short wavelengths. As to the group-mean spectral g, the slope of g with
501 wavelength in Type 1 is lower than in Types 2 and 3. The lower slope of the spectral g with a
502 higher g_{1020} in Type 1 represents the characteristic of urban-industrial, desert dust and marine
503 aerosols [*Dubovik et al.,* 2002a]. On the other hand, a case (1 April 2007) of Type 3 shows a
504 pronounced decrease of the g to the relatively low values (from g_{440} = 0.71 to g_{1020} = 0.52)
505 which corresponds to the features of biomass-burning aerosols [*Dubovik et al.,* 2002a].
506
507 **4.5. Aerosol Radiative Effect and Heating Rate**
508 The scatter plots of the daily mean $DARE_{TOA}$ and $DARE_{SFC}$ vs. τ at 500 nm are shown
509 in Figure 8. Straight lines indicate the linear regressions. Each point represents one day.

Circles represent radiative calculations on those days with daily-mean spectral τ, ω and g. Crosses represent calculations on those days where there are only daily-mean spectral τ, but no daily-mean spectral ω and g. Group-mean spectral ω and g are applied in the calculations. Squares represent calculations on those days where there are daily-mean spectral τ and g, but no daily-mean spectral ω. The group-mean spectral ω are applied in the calculations. The DARE is highly linearly correlated with τ_{500nm} with a negative correlation coefficient of > 0.93 for all types of aerosol vertical distributions, indicating that DARE can be reliably estimated from column-integrated τ_{500nm}. However, some points show a significant deviation from the linear regression which is related to the broad ranges of observed ω and g, especially the $DARE_{SFC}$ in Type 3. The large negative deviation of the $DARE_{SFC}$ from the linear regression on 1 April 2007 (Figure 8f) is due to the small ω and g (Figures 7c and 7f). On the other hand, the case of 14 October 2006 with large ω and g shows a weak negative $DARE_{SFC}$. The deviation of DARE from the linear regression can reach up to ±10 W m^{-2}.

At the TOA, the mean values of $DARE_{TOA}$ are -7.1, -11.6, and -11.2 W m^{-2} for Types 1, 2, and 3, respectively. The negative $DARE_{TOA}$ implies that the effect of the reflection of solar radiation due to aerosols is larger than the effect of absorption, and that the net effect is a cooling of the earth-atmosphere system. At the surface, the mean values of $DARE_{SFC}$ are -13.2, -20.3, and -18.7 W m^{-2} for Types 1, 2, and 3. The significant decrease of the solar radiation at the surface is enhanced by the absorption of solar radiation in the atmosphere due to aerosols. The absorption of solar radiation due to aerosols in the atmosphere, $DARE_{ATM}$, is 6.1, 8.7, and 7.5 W m^{-2} for Types 1–3, respectively.

533 The aerosol radiative efficiency (ARE) is defined as the change of DARE per unit
534 change of τ at 500 nm. This parameter is useful for quantifying and comparing aerosol
535 radiative effects at different places under a wide range of aerosol conditions [*Wang et al.*,
536 2007 and references therein]. We estimated ARE_{TOA} and ARE_{SFC} from the slopes of the linear
537 regressions shown in Figure 8, in which uncertainties can be explained by root-mean-square
538 (rms). The AREs for Types 1–3 are listed in Table 3. Values of ARE_{TOA} for these three types
539 are very close (~-23 W m^{-2}), indicating that the solar energy budget of the earth-atmosphere
540 system is not overly sensitive to the vertical distributions of aerosols over northern Taiwan.
541 Compared to ARE_{TOA}, the ARE_{SFC} and ARE_{ATM} show relative sensitivity to the vertical
542 distributions of aerosols, with the highest efficiency in Type 1 and the lowest efficiency in
543 Type 3.
544
545 A sensitivity study was performed to investigate how the aerosol vertical distributions
546 shaping the computations of ARE under the assumption of unified aerosol optical properties
547 (i.e., fixed column-integrated τ, column-mean ω, and g of moderate-absorbing aerosol) for
548 various profiles. As expected, the results show that all ARE_{TOA}, ARE_{SFC} and ARE_{ATM} increase
549 (i.e., larger negative values for the first two but larger positive value for the last ARE) when
550 more aerosols are elevated to higher levels in various profiles within thin-τ regime. These
551 increases are due to more downwelling solar irradiance available for aerosols to interact at
552 higher levels, leading to enhanced reflection at TOA and absorption in ATM (in turn, dimmed
553 transmission at SFC). However, as the degrees of freedom in aerosol properties increase (e.g.,
554 ω, g, τ, in addition to vertical distribution) in model simulations, the variation of AREs
555 becomes complex due to their competing nature for solar irradiance. Since most of aerosols

556 in Types 1–3 are confined in the lower atmosphere (i.e., below 3 km) with moderate
557 absorption, the values of ARE_{TOA} shown in Table 3 are weakly sensitive to aerosol vertical
558 distributions. When the variations of other aerosol properties (*cf*. Figures 3 and 7) come into
559 play (e.g., ω_λ dominant in Type–1 *vs*. Type–2, against their similar vertical distributions; or
560 larger variability of ω_λ and vertical distribution in Type–3 *vs*. Type–2), ARE_{SFC} coupled with
561 ARE_{ATM} reveal relatively larger variability, compared to ARE_{TOA}.
562
563 Although we have demonstrated that the vertical distribution of aerosols does not make
564 a significant difference in the estimation of ARE_{TOA}, it does provide information as to the
565 impact of aerosols on the vertical profile of the atmospheric heating rate. Figure 9 shows the
566 vertical distribution of the mean and one standard deviation of ΔQ (K day^{-1}) for Types 1–3. The
567 ΔQ profiles are similar to the σ profiles in Figure 3, with maximum values of 0.37, 0.41, and
568 0.26 K day^{-1} at around 700 m in height for Types 1–3, respectively. A larger σ implies a higher
569 aerosol concentration, and hence a stronger impact on ΔQ. The ΔQ of Type 3 is smaller than
570 those of Types 1 and 2 below 2 km, indicating that the upper-layer absorbing aerosol transport
571 enhances the upper-layer ΔQ at the expense of reducing the near-surface ΔQ. The nearly
572 constant ΔQ in the vertical implies a weaker impact on the stability and convection. On the
573 other hand, Types 1 and 2 have a larger ΔQ near the surface and, hence, have a larger impact on
574 convection than Type 3.
575
576 **4.6. Improving ARE Estimates for Two-layer Aerosol Transport**
577 The assumption of a constant column-mean ω and g throughout a two-layer aerosol

578 transport profile may cause an error in the radiative transfer calculations. The coexistence of
579 near-surface and upper-layer aerosol transport as shown from different source regions,
580 implies different ω and g in the vertical distribution. For example, the different ω in the
581 near-surface and upper layers has been observed using airborne measurements over Niamey
582 [*Osborne et al.,* 2008]. Except for aircraft measurement, the currently available retrieval
583 schemes based on ground measurements are unable to resolve vertical variations of ω and g.
584 Nevertheless, the AERONET measurements at a high mountain site at Lulin (23.51°N,
585 120.92°E; 2862 m MSL; ~180 km south of NCU), can provide useful information on the
586 optical properties of aerosols for the upper layers of Type 3 at NCU under the assumptions of
587 similar backward trajectories and aerosol sources [*Wai et al*., 2008, Figure 3].
588
589 The averaged ω and g of Lulin obtained from AERONET were used as surrogate to
590 improve the ARE estimates for the 2-layer aerosol transport. Due to the quality control
591 limitations of the AERONET inversion algorithm, only a few days of level 2 data [*Holben et*
592 *al.*, 2006] are available for 2007–2008. They occurred in March–May except for one day in
593 August. The available level 2 data give a 4-day averaged ω_{440nm} of 0.96 and a 16-day
594 averaged g_{440nm} of 0.7. Aerosols in the upper layer observed at Lilun exhibited a relatively
595 stronger scattering property and backward scattering, compared to Types 1–3. Here, we apply
596 aerosol optical properties derived from the Sun/sky radiometer at Lulin, to the upper-layer
597 aerosol transport in Type 3 and repeat the simulations of aerosol effect. In this case, the
598 process basically follows the vertical structure of Type 3, but the ω and g for the near-surface
599 aerosol layer were replaced with group-average values of Type 1 and 2 and for upper-layer
600 were replaced with averaged values of Lulin. As a result, the change in the vertical

601 distribution of the ω and g affects on the ARE calculations are shown in Table 3. Compared
602 to the results of Type 3 in Table 3, the redistributions of ω and g in the vertical profiles
603 enhance the negative ARE_{SFC} (surface cooling, ~-3 W m^{-2}) and the positive ARE_{ATM}
604 (atmosphere heating, ~3 W m^{-2}), but have only a minor influence on ARE_{TOA}. In addition, the
605 vertical distribution of ΔQ shows an enhanced ΔQ by up to 0.2 K day^{-1} in the surface layer
606 when near-surface aerosol replaced with the group-mean aerosol ω and g of Types 1 and 2
607 (shown in Figure 9c). These preliminary results encourage us to approach the 2-layer aerosol
608 transport problems in the future with case studies using the data from EPA-NCU and the Lulin
609 sites.
610
611 **5. Conclusions**
612 In this study, we presented a synergistic process to determine the vertical distributions of
613 aerosol optical properties and the impact of aerosols on solar heating using ground-based
614 remote-sensing (Micro-pulse lidar and Sun/sky radiometers) and a radiative transfer model.
615 The MPL and Sun/sky radiometer data were taken from observations at a rural site in
616 northern Taiwan and covered a period of three years (2005–2007).
617
618 To simplify the complex characteristics of the aerosol vertical distribution,
619 lidar-retrieved aerosol extinction profiles were classified into three types with common
620 characteristics of near-surface aerosol transport. These three types of aerosol profiles account
621 for 76% of the total data base. In general, the common near-surface aerosol transport (0 to 2
622 km) is related to the northerly air mass with possible long-range transport of aerosols during
623 wintertime. The upper-layer aerosol transport (2 to 4 km) is caused by the convective

624 mixing/dispersion of aerosol in the free atmosphere.

625

626 The columnar aerosol optical properties show that the aerosols in this region are
627 dominated by fine mode (Ångström exponent = ~1.40) and moderately absorbing aerosols (ω
628 = ~0.93 and g = ~0.73 at 440 nm), which are typical of urban-industrial aerosols [*Dubovik et*
629 *al.,* 2002a]. However, frequent perturbations due to desert dust, biomass-burning or mixed
630 aerosols suggest a diversity of aerosol types over the downwind area of the Asian continent.
631 Compared to the ω in the upwind areas (China and Korea), the higher ω in northern Taiwan
632 suggests that anthropogenic aerosols transported near the ocean surface are likely to
633 experience hydroscopic growth. The column-integrated aerosol optical thickness at 500 nm
634 (τ_{500nm}) ranges from 0.1 to 0.6 for near-surface aerosol transport, but can be doubled in the
635 presence of upper-layer aerosol transport.

636

637 Absorbing aerosols have the effect of warming the atmosphere and cooling the surface.
638 The sensitivity of solar radiation to a unit change of τ_{500nm}, referred to aerosol radiative
639 efficiency (ARE), was computed at the top of the atmosphere (ARE_{TOA}) and at the surface
640 (ARE_{SFC}). The ARE_{TOA} is not sensitive to the vertical distributions of aerosols, and is
641 approximately -23 W m^{-2} for the three types of aerosol profiles. On the other hand, the
642 ARS_{SFC} is relatively sensitive to the vertical distribution of aerosols, and is -44.3, -40.6 and
643 -39.7 W m^{-2} for the near-surface, mixed and two-layer transport types, respectively. The
644 difference is caused primarily by the difference in ω; surface transport type aerosols have the
645 smallest ω, and the two-layer transport type aerosols have the largest ω. Correspondingly, the
646 impact of aerosols on the vertical profile of solar heating is the largest for the near-surface

transport type and the smallest for the two-layer transport type. Since any changes of solar heating in the atmosphere and at the surface affect the stability of the atmosphere, different aerosol transport type will have different impact on the atmospheric stability, convection, and regional climate.

The coexistence of near-surface and upper-layer aerosol transports infers different aerosol characteristics in the vertical distribution. This study introduce a method, using Sun/sky radiometer observation at the high-altitude station, Lulin (2862 m), to further assist in estimating the upper-layer aerosol optical properties (ω and g) and improve the ARE calculations for the two-layer transport type of aerosols. Using the proposed method, the recalculated ARE_{SFC} and ARE_{ATM} are enhanced by 3 W m^{-2}, and the solar heating is enhanced by up to 0.2 K day^{-1} in the surface layers. This analysis shows the sensitivity of the vertical distribution of aerosol optical properties for estimating the aerosol radiative effect.

Acknowledgments

This work was supported by the National Science Council of Taiwan under contracts No. 97-2752-M-008-011-PAE, 96-2752-M-008-007-PAE, 97-2745-M-008-010, and 96-2745-M-008-005, and by the Taiwan Environmental Protection Administration under contracts No EPA-97-U1L1-02-101 and EPA-98-FA11-03-A015. The NASA MPLNET and AERONET are funded by the NASA Earth Observing System and Radiation Sciences Program. The authors gratefully acknowledge the NOAA Air Resources Laboratory for the provision of the HYSPLIT transport and dispersion model used in this publication. Special thanks to the scientists (NASA/GSFC) and technicians (NCU) responsible for consulting, operating and maintaining the instrumentation that generated this high-quality data set and ultimately enabled this paper to be written; these colleagues include Tom Eck, Timothy Berkoff, James Campbell, Larry Belcher, Ferret Kuo, and Eric Chia.

References

Bey, I., D. J. Jacob, Jennifer. A. Logan, and R. M. Yantosca (2001), Asian chemical outflow to the Pacific in spring: Origins, pathways, and budgets, *J. Geophys. Res.*, 106(D19), 23,097–23,113.

Campbell, J. R., D. L. Hlavka, E. J. Welton, C. J. Flynn, D. D. Turner, J. D. Spinhirne, V. S. Scott, and I. H. Hwang (2002), Full-Time, Eye-Safe Cloud and Aerosol Lidar Observation at Atmospheric Radiation Measurement Program Sites: Instruments and Data Processing, *J. Atmos. Oceanic Technol.*, 19, 431-442.

Campbell, J. R., E. J. Welton, J. D. Spinhirne, Q. Ji, S.-C. Tsay, S. J. Piketh, M. Barenbrug, and B. N. Holben (2003), Micropulse lidar observations of tropospheric aerosols over northeastern South Africa during the ARREX and SAFARI 2000 dry season experiments, *J. Geophys. Res.*, 108(D13), 8497, doi:10.1029/2002JD002563.

CCSP (2009), *Atmospheric Aerosol Properties and Climate Impacts,* A Report by the U.S. Climate Change Science Program and the Subcommittee on Global Change Research. [Mian Chin, Ralph A. Kahn, and Stephen E. Schwartz (eds.)]. National Aeronautics and Space Administration, Washington, D.C., USA, 128 pp.

Chiang, C.-W., W.-N. Chen, W.-A. Liang, S. K. Das, J.-B. Nee (2007), Optical properties of tropospheric aerosols based on measurements of lidar, sun-photometer, and visibility at Chung-Li (25˚N, 121˚E), *Atmos. Environ.*, 41, 4128-4137.

Chou, M.-D., and K. T. Lee (1996), Parameterizations for the absorption of solar radiation by water vapor and ozone, *J. Atmos. Sci.*, 53, 1203–1208.

Chou, M. D., and M. J. Suarez (1999), A solar radiation parameterization for atmospheric studies, *NASA Tech. Memo., NASA-TM-1999-10460,* vol. 15, 40pp.

Chou, M.-D., P.-H. Lin, P.-L. Ma, and H.-J. Lin (2006), Effects of aerosols on the surface solar radiation in a tropical urban area, *J. Geophys. Res.*, 111, D15207, doi:10.1029/2005JD006910.

Draxler, R. R. (1996), Boundary layer isentropic and kinematic trajectories during the August 1993 North Atlantic Regional Experiment Intensive, *J. Geophys. Res.*, 101(D22), 29,255–29,268.

Draxler, R. R., and G. Rolph (2003), HYSPLIT4 (HYbrid Single-Particle Lagrangian Integrated Trajectory) model, Air Resour. Lab., Natl. Oceanic and Atmos. Admin., Silver Spring, Md. (Available at http://www.arl.noaa.gov/ready/hysplit4.html).

Dubovik, O., and M. D. King (2000), A flexible inversion algorithm for retrieval of aerosol optical properties from Sun and sky radiance measurements, *J. Geophys. Res.*, 105(D16), 20,673–20,696.

Dubovik, O., B. N. Holben, T. F. Eck, A. Smirnov, Y. J. Kaufman, M. D. King, D. Tanre, and I. Slutsker (2002a), Variability of absorption and optical properties of key aerosol types observed in worldwide locations, *J. Atmos. Sci.,* 59, 590-608.

Dubovik, O., B. N. Holben, T. Lapyonok, A. Sinyuk, M. I. Mishchenko, P. Yang, and I. Slutsker (2002b), Non-spherical aerosol retrieval method employing light scattering by

spheriods, *Geophys. Res. Lett.,* 29, 54-1 - 54-4.

Dubovik, O., et al. (2006), Application of spheroid models to account for aerosol particle nonsphericity in remote sensing of desert dust, *J. Geophys. Res.*, 111, D11208, doi:10.1029/2005JD006619.

Eck, T. F., et al. (2005), Columnar aerosol optical properties at AERONET sites in central eastern Asia and aerosol transport to the tropical mid-Pacific, *J. Geophys. Res.*, 110, D06202, doi:10.1029/2004JD005274.

Hayasaka, T., S. Satake, A. Shimizu, N. Sugimoto, I. Matsui, K. Aoki, and Y. Muraji (2007), Vertical distribution and optical properties of aerosols observed over Japan during the Atmospheric Brown Clouds–East Asia Regional Experiment 2005, *J. Geophys. Res.*, 112, D22S35, doi:10.1029/2006JD008086.

Haywood, J. M., and V. Ramaswamy (1998), Global sensitivity studies of the direct radiative forcing due to anthropogenic sulfate and black carbon aerosols, *J. Geophys. Res.*, 103(D6), 6043– 6058.

He, Q., C. Li, J. Mao, A. K.-H. Lau, and D. A. Chu (2008), Analysis of aerosol vertical distribution and variability in Hong Kong, *J. Geophys. Res.*, 113, D14211, doi:10.1029/2008JD009778.

Holben, B. N., T. F. Eck, I. Slutsker, D. Tanre, J. P. Buis, A. Setzer, E. Vermote, J. A. Reagan, Y. J. Kaufman, T. Nakajima, F. Lavenu, I. Jankowiak and A. Smirnov (1998), AERONET: a federated instrument network and data archive for aerosol characterization, *Rem. Sens. Environ.*, 66, 1-16.

Holben, B. N., T. F. Eck, I. Slutsker, A. Smirnov, A. Sinyuk, J. Schafer, D. Giles and O. Dubovik (2006), Aeronet's Version 2.0 quality assurance criteria, *Proc. SPIE*, 6408, 64080Q, doi:10.1117/12.706524.

Hsu, N. C., J. R. Herman, and S.-C. Tsay (2003), Radiative impacts from biomass burning in the presence of clouds during boreal spring in southeast Asia, *Geophys. Res. Lett.*, 30(5), 1224, doi:10.1029/2002GL016485.

Hsu, N. C., S.-C. Tsay, M. D. King and J. R. Herman (2004), Aerosol properties over bright-reflecting source regions, *IEEE Trans. Geosci. Rem. Sens.*, 42, 557-569.

Hsu, N. C., S.-C. Tsay, M. D. King and J. R. Herman (2006), Deep Blue retrievals of Asian aerosol properties during ACE-Asia, *IEEE Trans. Geosci. Rem. Sens.*, 44, 3180-3195.

Intergovernmental Panel on Climate Chang (IPCC) (2007), Climate Change 2007, Working Group I Report "The Physical Science Basis", edited by S. Solomon et al., *Cambridge Univ. Press*, New York.

Johnson, B. T., B. Heese, S. A. McFarlane, P. Chazette, A. Jones, and N. Bellouin (2008), Vertical distribution and radiative effects of mineral dust and biomass burning aerosol over West Africa during DABEX, *J. Geophys. Res.*, 113, D00C12, doi:10.1029/2008JD009848.

Kalnay, E., et al. (1996), The NCEP/NCAR 40-year reanalysis project, *Bull. Amer. Meteor. Soc.,* 77, 437-470.

754 Kaufman, Y. J., D. Tanre, H. R. Gordon, T. Nakajima, J. Lenoble, R. Frouin, H. Grassl, B. M.
755 Hermann, M. D. King, and P. M. Teillet (1997a), Passive remote sensing of tropospheric
756 aerosol and atmospheric correction for the aerosol effect, *J. Geophys. Res.*, 102,
757 16,815–16, 830, doi:10.1029/97JD01496.

758 Kaufman, Y. J., D. Tanré, L. A. Remer, E. Vermote, A. Chu and B. N. Holben (1997b),
759 Remote sensing of tropospheric aerosol from EOS-MODIS over the land using dark
760 targets and dynamic aerosol models, *J. Geophys. Res.*, 102, 17051-17067.

761 Levy, R. C., L. A. Remer, S. Mattoo, E. F. Vermote and Y. J. Kaufman (2007),
762 Second-generation operational algorithm: Retrieval of aerosol properties over land from
763 inversion of Moderate Resolution Imaging Spectroradiometer spectral reflectance, *J.*
764 *Geophys. Res.*, 112, D13211, doi:10.1029/2006JD007811.

765 Liang, Q., L. Jaegle´, D. A. Jaffe, P. Weiss-Penzias, A. Heckman, and J. A. Snow (2004),
766 Long-range transport of Asian pollution to the northeast Pacific: Seasonal variations and
767 transport pathways of carbon monoxide, *J. Geophys. Res.*, *109,* D23S07,
768 doi:10.1029/2003JD004402.

769 Liu, C.-M., C.-Y. Young, and Y.-C. Lee (2006), Influence of Asian dust storms on air quality
770 in Taiwan, *Sci. of the Total Environ.*, 368, 884-897.

771 McFarlane, S. A., E. I. Kassianov, J. Barnard, C. Flynn, and T. P. Ackerman (2009), Surface
772 shortwave aerosol radiative forcing during the Atmospheric Radiation Measurement
773 Mobile Facility deployment in Niamey, Niger, *J. Geophys. Res.*, 114, D00E06,
774 doi:10.1029/2008JD010491.

775 Murayama, T., D. Müller, K. Wada, A. Shimizu, M. Sekiguchi, and T. Tsukamoto (2004),
776 Characterization of Asian dust and Siberian smoke with multi-wavelength Raman lidar
777 over Tokyo, Japan in spring 2003, *Geophys. Res. Lett.*, 31, L23103,
778 doi:10.1029/2004GL021105.

779 Osborne, S. R., B. T. Johnson, J. M. Haywood, A. J. Baran, M. A. J. Harrison, and C. L.
780 McConnell (2008), Physical and optical properties of mineral dust aerosol during the
781 Dust and Biomass-burning Experiment, *J. Geophys. Res.*, 113, D00C03,
782 doi:10.1029/2007JD009551.

783 Schaaf, C. B., et al. (2002), First Operational BRDF, Albedo and Nadir Reflectance Products
784 from MODIS*, Remote Sens. Environ.*, 83, 135-148.

785 Schmid, B., R. Ferrare, C. Flynn, R. Elleman, D. Covert, A. Strawa, E. Welton, D. Turner, H.
786 Jonsson, J. Redemann, J. Eilers, K. Ricci, A. G. Hallar, M. Clayton, J. Michalsky, A.
787 Smirnov, B. Holben, and J. Barnard (2006), How well do state-of-the-art techniques
788 measuring the vertical profile of tropospheric aerosol extinction compare?, *J. Geophys.*
789 *Res.*, 111, D05S07, doi:10.1029/2005JD005837.

790 Seinfeld J. H. (1986), *Atmospheric chemistry and physics of air pollution*, 738 pp., Wiley,
791 New York, USA.

792 Smirnov A., B. N. Holben, T. F. Eck, O. Dubovik, and I. Slutsker (2000), Cloud screening
793 and quality control algorithms for the AERONET database, *Remote Sens. Environ.*, 73,
794 337-349.

795 Spinhirne, J. D., J. A. R. Rall, and V. S. Scott (1995), Compact eye safe lidar systems, *Rev.*
796 *Laser Eng.,* 23, 112-118.

797 Streets, D. G., et al. (2003), An inventory of gaseous and primary aerosol emissions in Asia in
798 the year 2000, *J. Geophys. Res.*, 108(D21), 8809, doi:10.1029/2002JD003093.

799 Stull, R. B. (1988), *An introduction to boundary layer meteorology*, Kluwer Academic
800 Pulishers, Dordrecht, 2-3.

801 Tanré, D., Y. J. Kaufman, M. Herman and S. Mattoo (1997), Remote sensing of aerosol over
802 oceans from EOS-MODIS**,** *J. Geophys. Res.,* 102, 16971-16988.

803 Wai, K. M., N.-H. Lin, S.-H. Wang, and Y. Dokiya (2008), Rainwater chemistry at a
804 high-altitude station, Mt. Lulin, Taiwan: Comparison with a background station, Mt. Fuji,
805 *J. Geophys. Res.*, 113, D06305, doi:10.1029/2006JD008248.

806 Wang, S.-H., N.-H. Lin, M.-D. Chou, and J.-H. Woo (2007), Estimate of radiative forcing of
807 Asian biomass-burning aerosols during the period of TRACE-P, *J. Geophys. Res.*, 112,
808 D10222, doi:10.1029/2006JD007564.

809 Welton, E. J., et al. (2000), Ground-based lidar measurements of aerosols during ACE-2:
810 Instrument description, results, and comparisons with other ground-based and airborne
811 measurement, *Tellus 52B*, 636-651.

812 Welton, E. J., J. R. Campbell, J. D. Spinhirne, and V. S. Scott (2001), Global monitoring of
813 clouds and aerosols using a network of micro-pulse lidar systems, in Lidar Remote
814 Sensing for Industry and Environmental Monitoring, U. N. Singh, T. Itabe, N. Sugimoto,
815 (eds.), *Proc. SPIE*, 4153, 151-158.

816 Welton, E. J., K. J. Voss, P. K. Quinn, P. J. Flatau, K. Markowicz, J. R. Campbell, J. D.
817 Spinhirne, H. R. Gordon, and J. E. Johnson (2002), Measurements of aerosol vertical
818 profiles and optical properties during INDOEX 1999 using micropulse lidars, *J. Geophys.*
819 *Res.*, 107(D19), 8019, doi:10.1029/2000JD000038.

820

821 **Figure captions**

822 Figure 1. Histogram of the number of days in the month for: (a) AERONET and (b)
823 MPLNET data sets. The light gray and dark gray color bars present level 1 and level 2 data,
824 respectively, for both of the AERONET and the MPLNET data sets. The black color bar
825 presents the MPLNET level 2 dataset with data from Types 1–3 only.

826 Figure 2. Examples of aerosol extinction (km^{-1}) profiles obtained by MPL at EPA-NCU for:
827 (a) Type 1 (12-Nov-2006), (b) Type 2 (13-Feb-2007) and (c) Type 3 (15-Oct-2006). The blue
828 line is the daily-averaged profile and the red lines present all profiles on that day. Below
829 375.0 m, no readings are shown due to the near-field observation limits of MPL. Examples of
830 the ambient (Square point) and dew point (dot point) temperature ($^{\circ}C$) profiles obtained by
831 Taipei sounding station (~ 30 km north of NCU) at 00UTC for: (d) Type 1 (12-Nov-2006), (e)
832 Type 2 (13-Feb-2007) and (f) Type 3 (15-Oct-2006). The dashed lines between two points
833 present continuously sampling in the vertical distribution, otherwise invalid values are noted.

834 Figure 3. Profiles of the mean aerosol extinction with one standard deviation derived from the
835 MPLNET observations at EPA-NCU for (a) Type 1, (b) Type 2 and (c) Type 3, with
836 corresponding monthly total number of days for (d) Type 1, (e) Type 2 and (f) Type 3.

837 Figure 4. Five-day backward trajectories of NCU for (a) Type 1 starting at 500 m, (b) Type 2
838 starting at 500 m, (c) Type 3 starting at 500 m, (d) Type 2 starting at 2500 m, and (e) Type 3
839 starting at 2500 m. Each trajectory starts at 00 UTC. Trajectory altitudes (based on the mean
840 sea level, in meters) are denoted by the color scale.

841 Figure 5. Composite MODIS-Aqua aerosol Deep-Blue and Dark-Target retrievals of τ_{550nm}

842 averaged for (a) Type 1, (b) Type 2, and (c) Type 3. The third day before the case days based
843 on the potential pollution source regions has been applied in these plots.

844 Figure 6. Scatterplots of τ_{500nm} vs. $\alpha_{440–870nm}$ at NCU for (a) Type 1, (b) Type 2 and (c) Type 3.
845 The error bars indicate the one standard deviation.

846 Figure 7. The AERONET inversion data (ω and g) at 440, 675, 870, 1020 nm at NCU for (a)
847 ω of Type 1, (b) ω of Type 2, (c) ω of Type 3, (d) g of Type 1, (e) g of Type 2, and (f) g of
848 Type 3. The daily-mean spectral ω and g are shown as cross points and thin lines. The
849 group-mean spectral ω and g are shown as black circles and bold lines.

850 Figure 8. Scatterplots of DARE at TOA vs. τ at 500 nm for (a) Type 1, (b) Type 2, and (c)
851 Type 3. Scatterplots of DARE at the surface vs. τ_{500nm} for (d) Type 1, (e) Type 2, and (f) Type
852 3. Circles represent radiative calculations based on daily-mean spectral ω and g, crosses
853 represent data based on only group-mean spectral ω and g, and squares represent data based
854 on daily-mean spectral g and group-mean spectral ω.

855 Figure 9. The vertical distribution of the mean and one standard deviation of the impact of
856 aerosols on the atmospheric heating rate ΔQ (K day^{-1}) over NCU for (a) Type 1, (b) Type 2
857 and (c) Type 3 (red lines). The green line* and the blue line** show the improved ΔQ profiles
858 for Type 3. See Table 3 for detailed descriptions of * and **.

859 Table 1. The classification rules for daily mean aerosol extinction (σ) profiles

Type 1	1. The column-integrated τ_{527nm} greater than 0.1 2. No σ are detected above 6 km AGL* 3. A remarkable and isolated near surface aerosol layer
Type 2	1. Same as rules 1–3 in Type 1 2. Above the near surface aerosol layer, presenting a weaker aerosol layer with vertical aerosol mixing
Type 3	1. Same as rules 1–3 in Type 1 2. Above the near surface aerosol layer, presenting another remarkable and isolated aerosol layer 3. The joint between the two layers shows low σ

860 *According to long-term MPL observations of EPA-NCU, most atmospheric aerosols exist
861 below 6 km AGL at this site.

862

863

Table 2. The aerosol optical thickness (τ) at 500 nm, Ångström exponent (α) at 440 - 870 nm, single-scattering albedo (ω) at 440 nm, and asymmetry factor (g) at 440 nm retrieved from Sun/sky radiometer measurements

Type	Days	τ_{500nm}		$\alpha_{440–870nm}$		ω_{440nm}		g_{440nm}	
		mean	std	mean	std	mean	std	mean	std
Type 1	28	0.28	0.14	1.40	0.17	0.92	0.02	0.72	0.02
Type 2	51	0.45	0.22	1.40	0.18	0.95	0.02	0.73	0.02
Type 3	31	0.44	0.26	1.43	0.15	0.95	0.02	0.73	0.02

868 Table 3. Aerosol Radiative Efficiency (ARE) of TOA, ATM and SFC for Types 1–3.

	ARE_{TOA}	ARE_{ATM}	ARE_{SFC}
Type 1	-23.3	+21.0	-44.3
Type 2	-22.6	+18.0	-40.6
Type 3	-22.9	+16.8	-39.7
Type 3 (Lulin1*)	-23.1	+19.8	-42.9
Type 3 (Lulin2**)	-24.2	+16.9	-41.1

869 Unit: W m^{-2}

870 * Values of ω and g at the upper-layer and the near-surface layer of Type 3 were replaced with
871 the mean values from the Lulin site and Type 1, respectively.
872 ** Values of ω and g at the upper-layer and the near-surface layer of Type 3 were replaced
873 with the mean values from the Lulin site and Type 2, respectively.
874

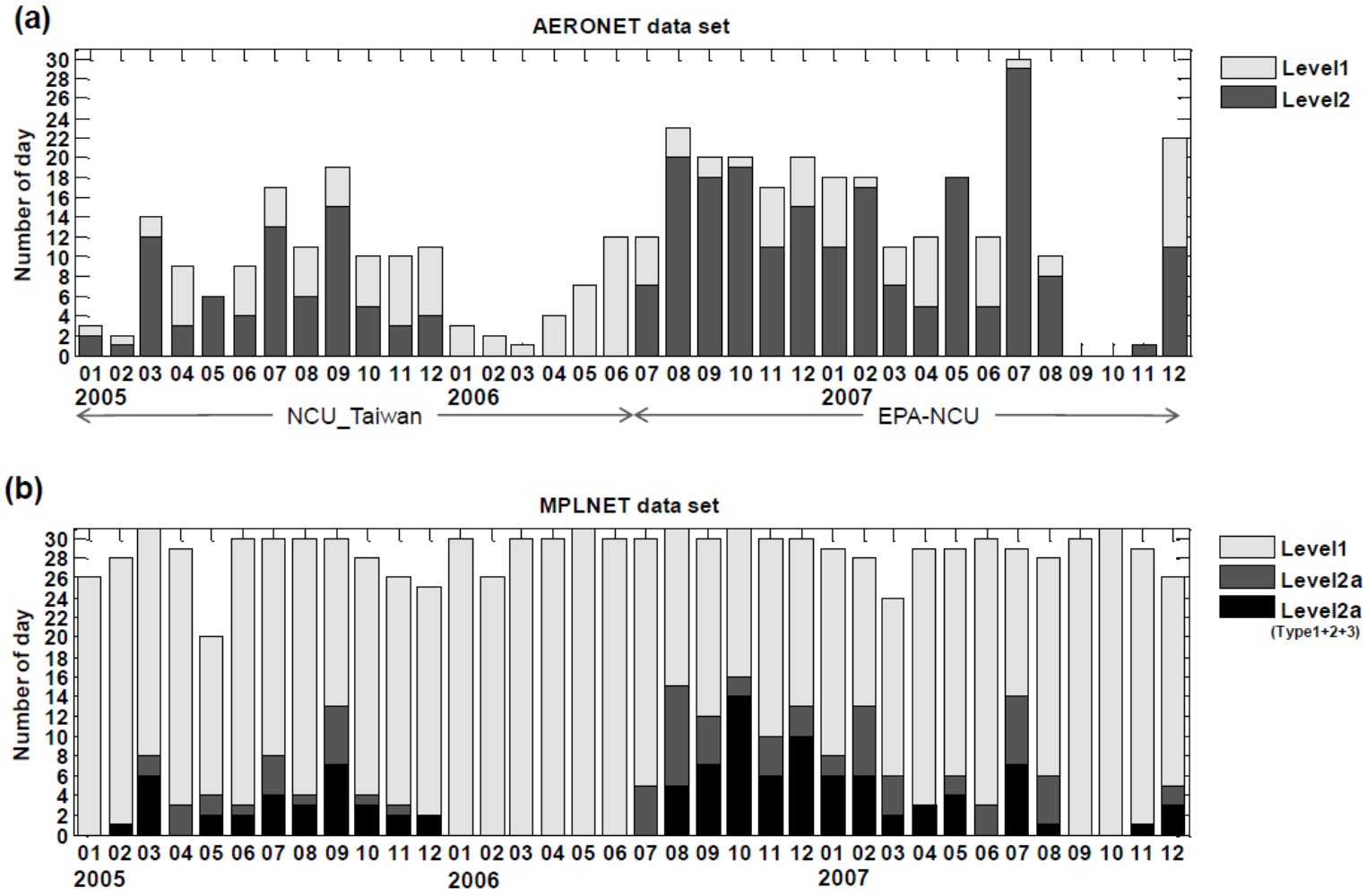

Figure 1. Histogram of the number of days in the month for: (a) AERONET and (b) MPLNET data sets. The light gray and dark gray color bars present level 1 and level 2 data, respectively, for both of the AERONET and the MPLNET data sets. The black color bar presents the MPLNET level 2 dataset with data from Types 1–3 only.

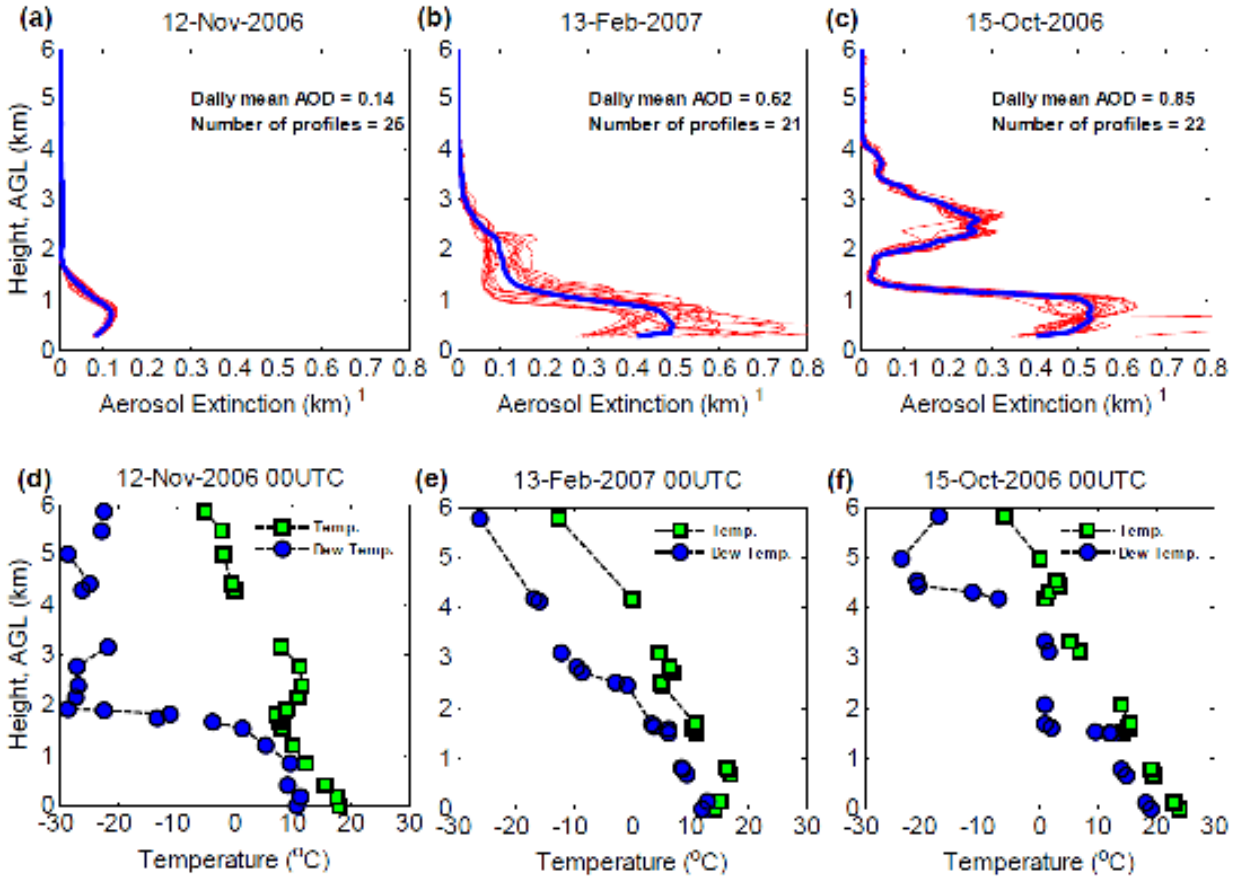

Figure 2. Examples of aerosol extinction (km^{-1}) profiles obtained by MPL at EPA-NCU for: (a) Type 1 (12-Nov-2006), (b) Type 2 (13-Feb-2007) and (c) Type 3 (15-Oct-2006). The blue line is the daily-averaged profile and the red lines present all profiles on that day. Below 375.0 m, no readings are shown due to the near-field observation limits of MPL. Examples of the ambient (Square point) and dew point (dot point) temperature (°C) profiles obtained by Taipei sounding station (~ 30 km north of NCU) at 00UTC for: (d) Type 1 (12-Nov-2006), (e) Type 2 (13-Feb-2007) and (f) Type 3 (15-Oct-2006). The dashed lines between two points present continuously sampling in the vertical distribution, otherwise invalid values are noted.

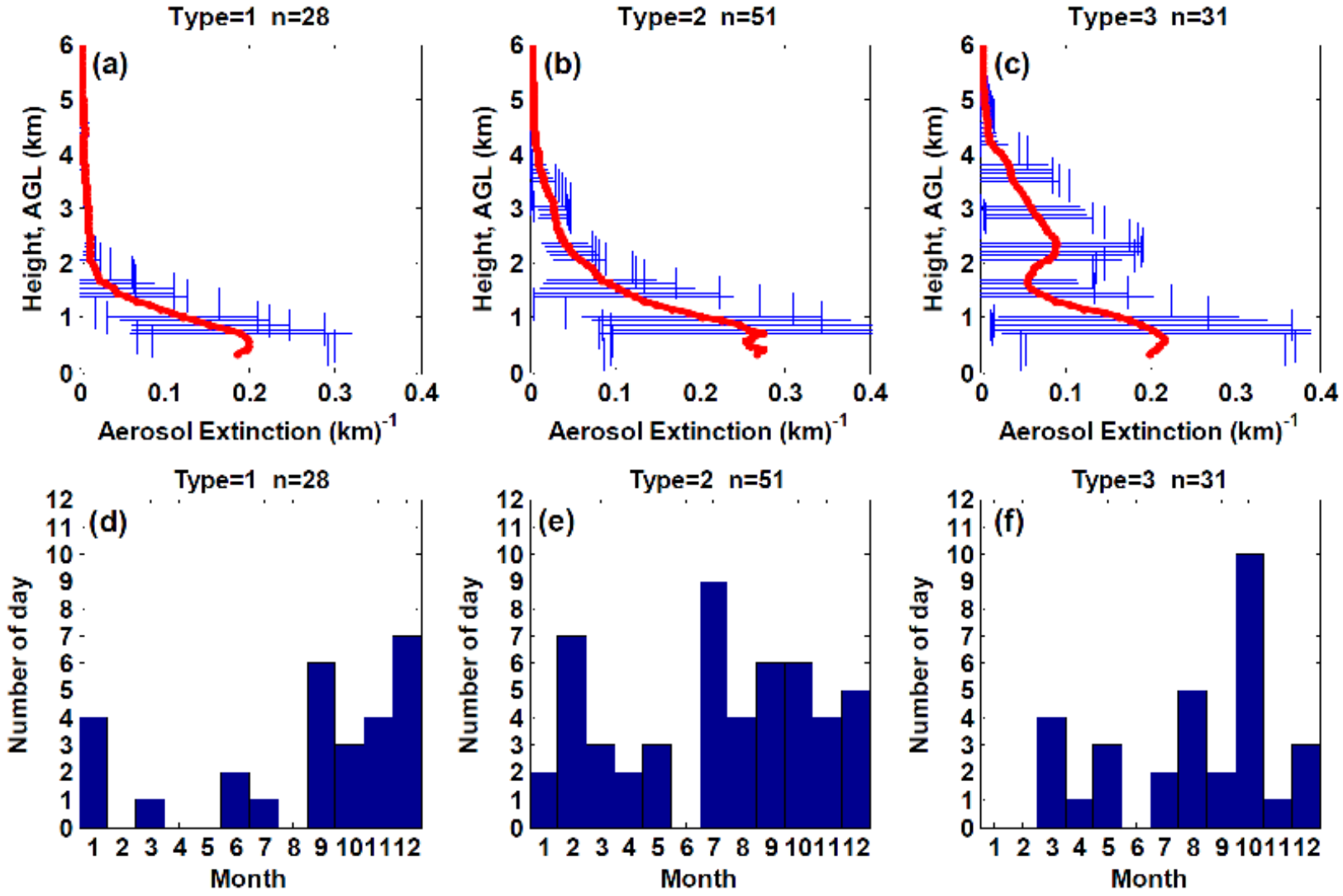

Figure 3. Profiles of the mean aerosol extinction with one standard deviation derived from the MPLNET observations at EPA-NCU for (a) Type 1, (b) Type 2 and (c) Type 3, with corresponding monthly total number of days for (d) Type 1, (e) Type 2 and (f) Type 3.

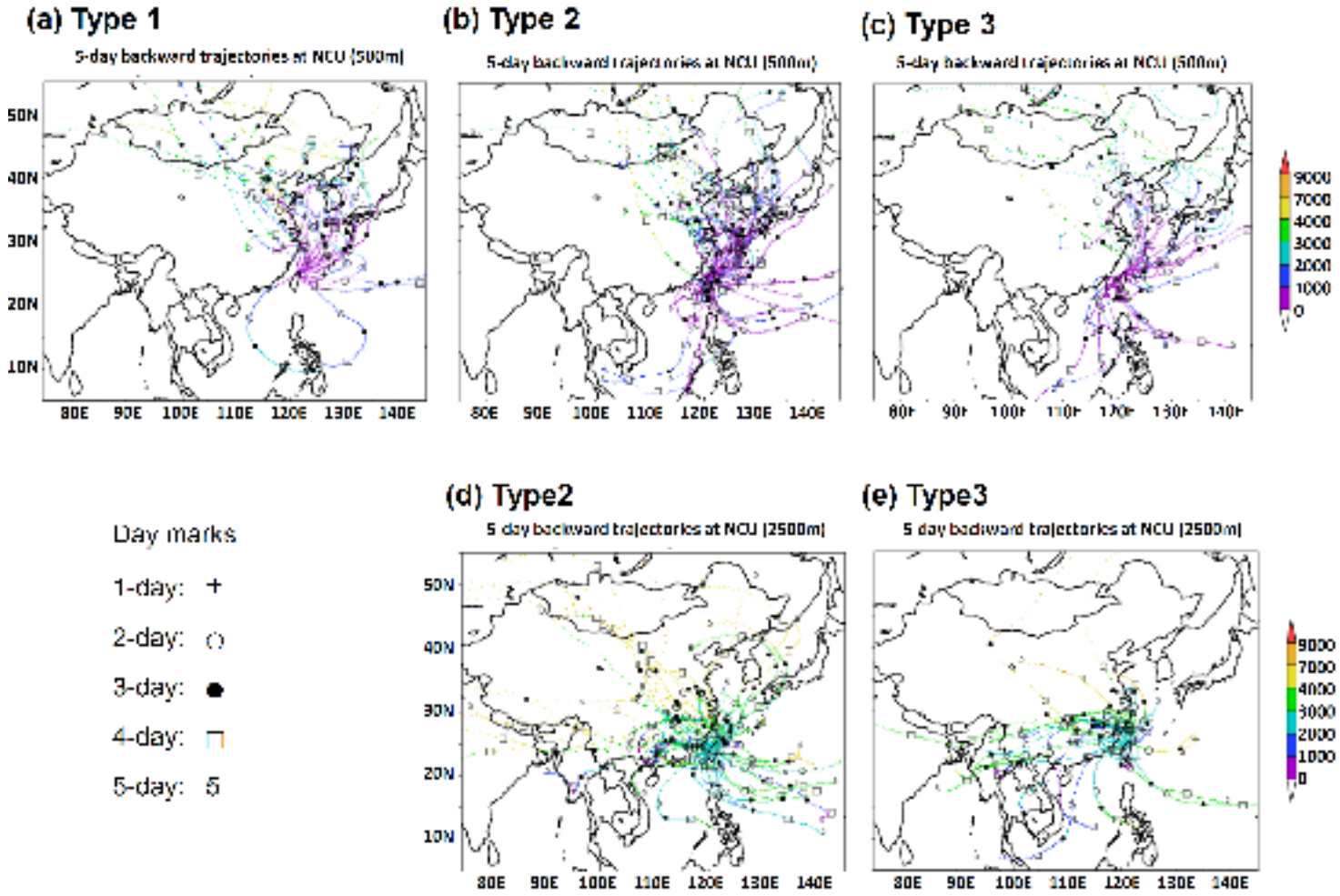

Figure 4. Five-day backward trajectories of NCU for (a) Type 1 starting at 500 m, (b) Type 2 starting at 500 m, (c) Type 3 starting at 500 m, (d) Type 2 starting at 2500 m, and (e) Type 3 starting at 2500 m. Each trajectory starts at 00 UTC. Trajectory altitudes (based on the mean sea level, in meters) are denoted by the color scale.

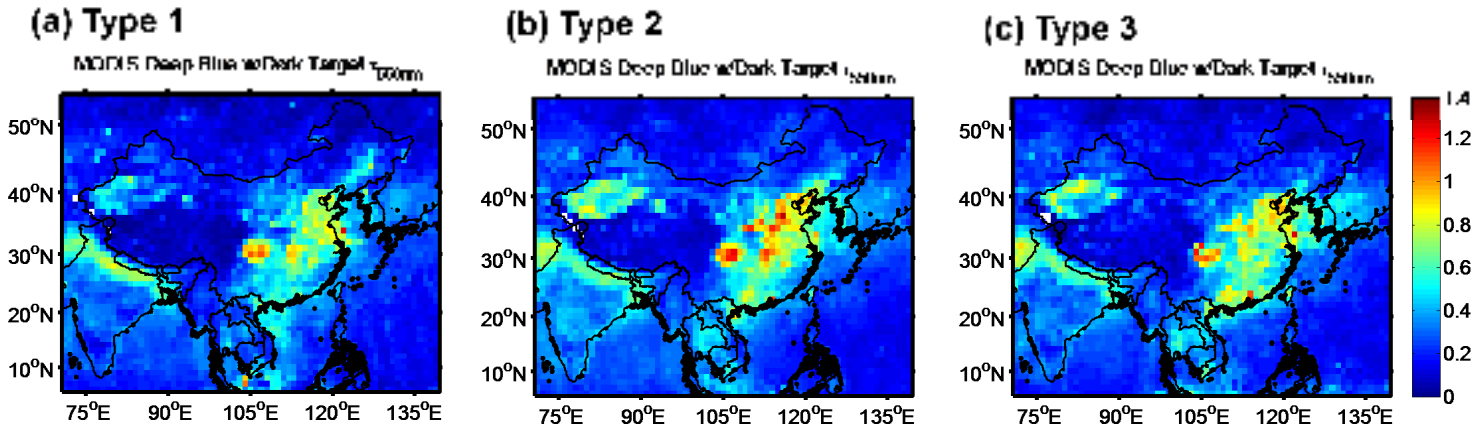

895

896 Figure 5. Composite MODIS-Aqua aerosol Deep-Blue and Dark-Target retrievals of τ_{550nm} averaged for (a) Type 1, (b) Type 2, and (c) Type 3.

897 The third day before the case days based on the potential pollution source regions has been applied in these plots.

898

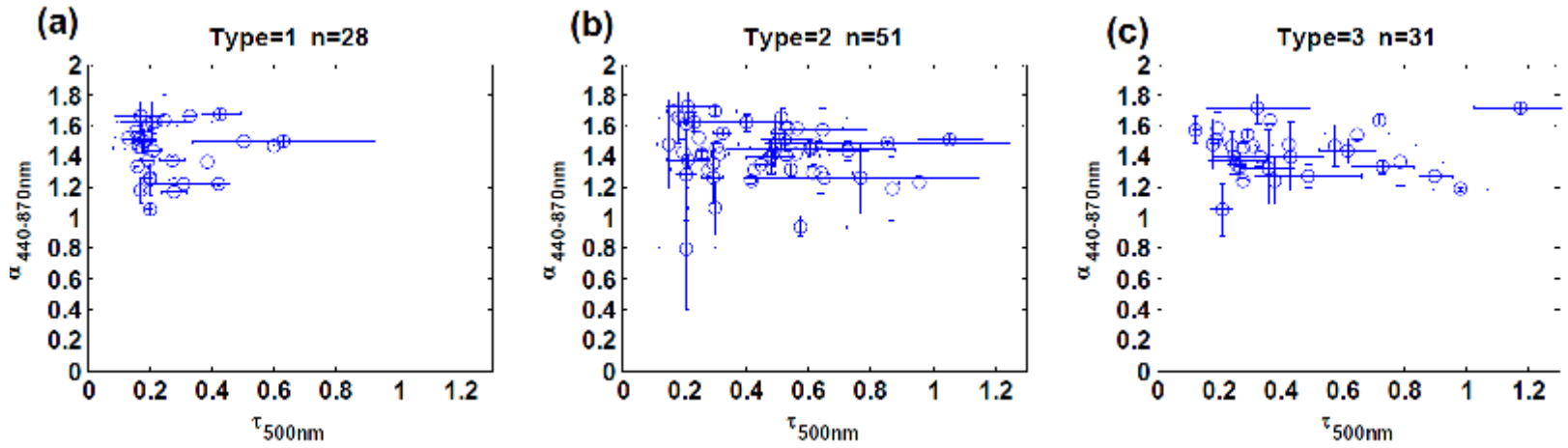

899

900 Figure 6. Scatterplots of τ_{500nm} vs. $\alpha_{440-870nm}$ at NCU for (a) Type 1, (b) Type 2 and (c) Type 3. The error bars indicate the one standard deviation.

901

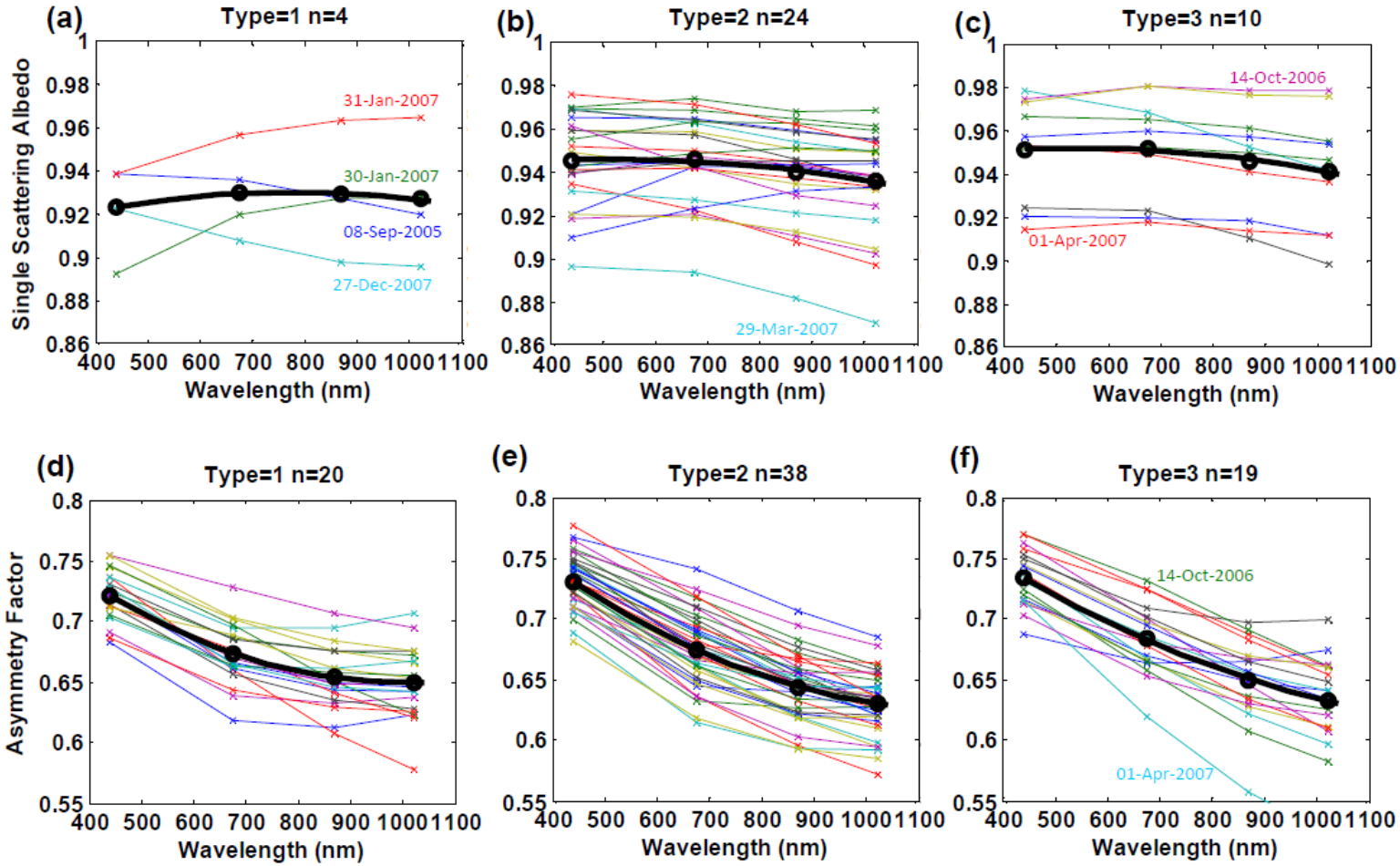

Figure 7. The AERONET inversion data (ω and g) at 440, 675, 870, 1020 nm at NCU for (a) ω of Type 1, (b) ω of Type 2, (c) ω of Type 3, (d) g of Type 1, (e) g of Type 2, and (f) g of Type 3. The daily-mean spectral ω and g are shown as cross points and thin lines. The group-mean spectral ω and g are shown as black circles and bold lines.

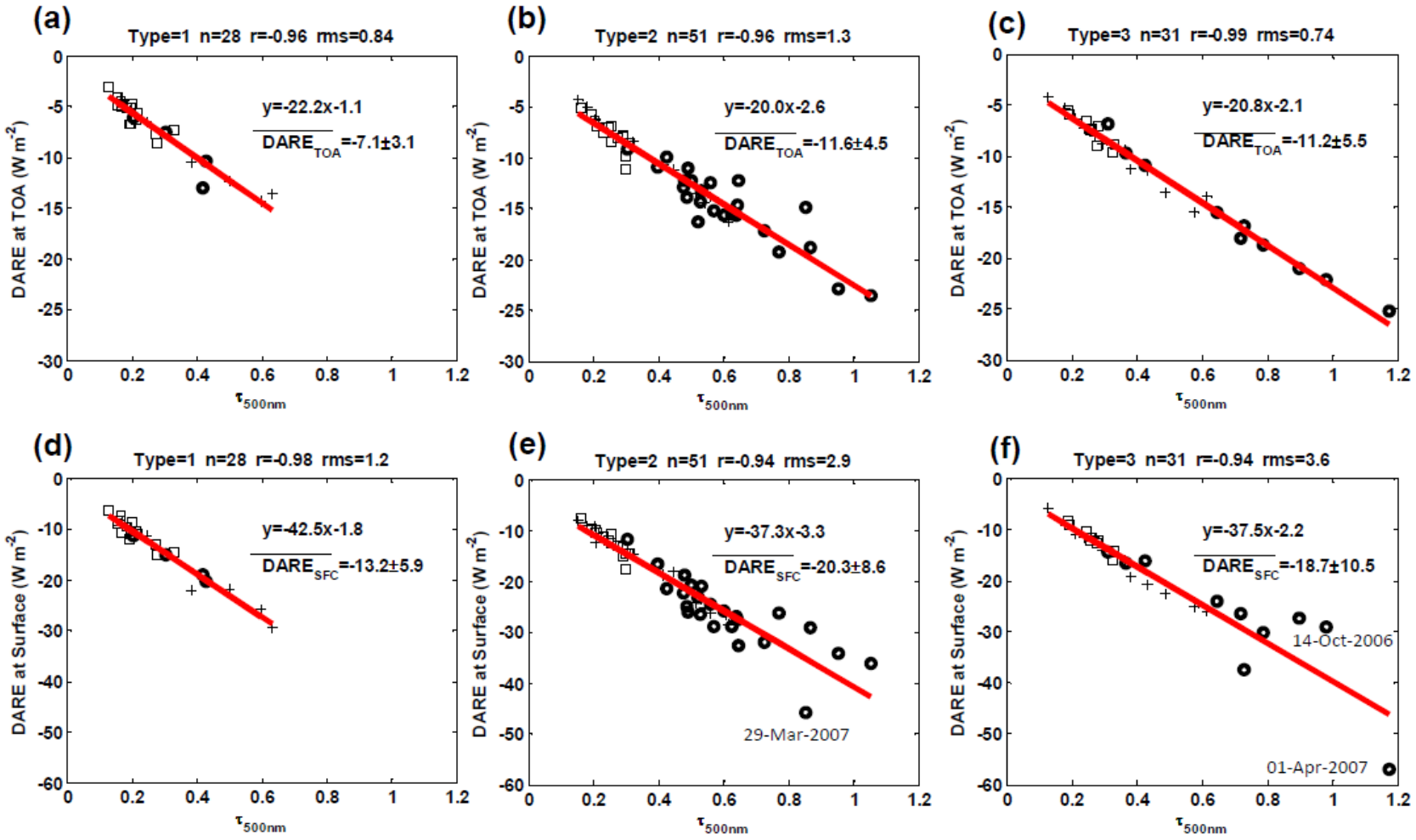

Figure 8. Scatterplots of DARE at TOA vs. τ at 500 nm for (a) Type 1, (b) Type 2, and (c) Type 3. Scatterplots of DARE at the surface vs. τ_{500nm} for (d) Type 1, (e) Type 2, and (f) Type 3. Circles represent radiative calculations based on daily-mean spectral ω and g, crosses represent data based on only group-mean spectral ω and g, and squares represent data based on daily-mean spectral g and group-mean spectral ω.

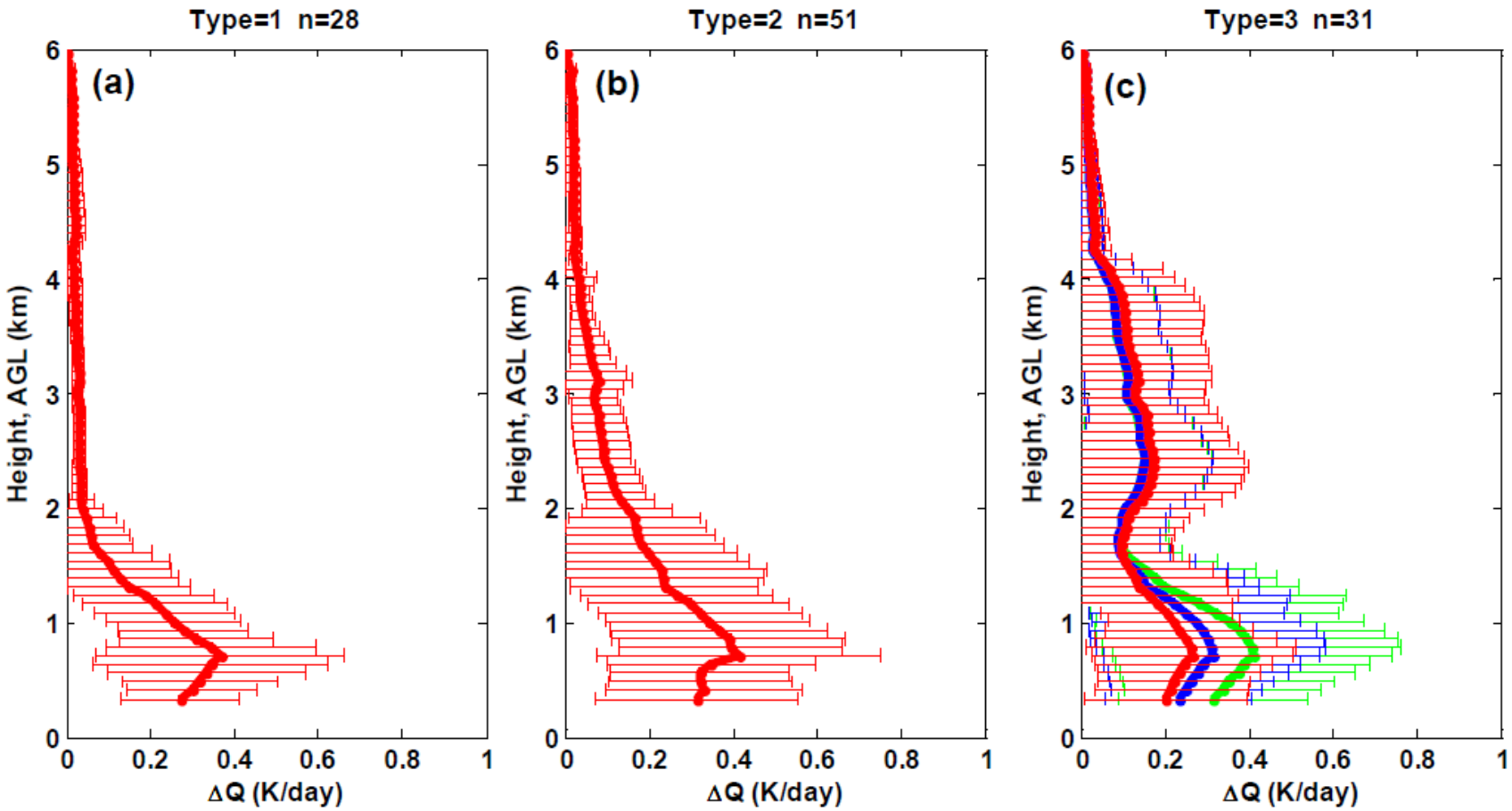

910

911 Figure 9. The vertical distribution of the mean and one standard deviation of the impact of aerosols on the atmospheric heating rate ΔQ (K day^{-1})
912 over NCU for (a) Type 1, (b) Type 2 and (c) Type 3 (red lines). The green line* and the blue line** show the improved ΔQ profiles for Type 3.
913 See Table 3 for detailed descriptions of * and **.